Analytical solution to a nonseparable interaction model for a one-dimensional fluid of anisotropic molecules near a hard wall

Bruno Martínez-Haya
Departamento de Química Física, Facultad de Química, Universidad Complutense, 28040 Madrid, Spain

Juan M. Pastor
Departamento de Física Fundamental, Facultad de Ciencias, Universidad Nacional de Educación a Distancia, 28040 Madrid, Spain

José A. Cuesta
Grupo Interdisciplinar de Sistemas Complicados, Departamento de Matemáticas, Universidad Carlos III, 28911 Leganes, Madrid, Spain
(Received 15 September 1998)

We introduce a one-dimensional fluid model of anisotropic molecules near a hard wall having a nonseparable interaction and yet being analytically solvable. We compute radial and angular profiles of the particles as well as the equation of state of the system. The model is worked out for two different hard core potentials and the results are compared to a Monte Carlo simulation. We find that the model provides a very accurate description of the system except in the limit of low pressure and large particle anisotropy where the fluctuation of the particle orientations become too large. In particular, the nonseparable character of the particle interaction potential leads to a coupling of the radial and angular parts of the one-body distribution that allows for a study of the correlation between the alignment of the particles and their distance to the hard wall. This feature constitutes a remarkable qualitative improvement with respect to any separable interaction model in which the radial and angular variables are necessarily decoupled. [S1063-651X(99)02602-1]

PACS number(s): 61.30.Cz, 61.30.Gd, 61.20.Ja, 05.70.Ce

I. INTRODUCTION

''Theoretical many-body physics ... is an art. The art ... is that of constructing simple solvable relevant models, whose solutions are simply expressed.'' With these words Percus [1] resumes a whole current of thought in physics that bases the understanding of physical systems upon the exact solution to simple, idealized models. One of these models is the keystone of statistical mechanics: the Ising model, whose exact solution is known in one and two dimensions. This model has given rise to a whole bunch of exactly solvable lattice models of different physical systems [2].

The physics of fluids has also benefited from this ''art.'' The fluid counterpart of the Ising model is the hard sphere fluid, which in one dimension is called the hard rod fluid [3]. Although known for more than a century, this model has provided relevant information only recently. The original works of Lord Rayleigh [3] and Tonks [4] provided the equation of state of this fluid. The distribution function of the homogeneous hard rod model was obtained half a century ago [5] and its direct correlation function did not appear until the 1970s [6]. However, perhaps the highest achievement with this model is Percus's obtention of its *exact* Helmholtz free-energy density functional [7]. This solution has proved crucial in the understanding of density functional theory [8], one of the most powerful analytical tools we currently have at our disposal to obtain the phase behavior of fluids.

The original hard rod model has been extended in different directions. A closely related model in the way towards two-dimensional fluids is the system of parallel hard squares in a narrow channel [9], which can be generalized to a multicomponent system of hard particles with a next-neighbor interaction [1]. An extension to include attractions is the fluid of adhesive hard rods, whose grand potential has been obtained as a functional of the density profile [7]. Associating hard rods have also been considered as a model of polymerization [10].

Fluids of anisotropic particles have also received attention in the context of solvable models. Basically there are two ways of introducing orientational degrees of freedom in one dimension (where, strictly speaking, rotations are excluded): Either we can restrict the center of mass of, say, ellipses to lay on a straight line but allow them to interact as two-dimensional objects or we can consider only their projections on the line and let particles interact through these projections. The former system captures an essential feature of fluids of anisotropic particles, namely, that positions and orientations are strongly coupled and hence it is difficult to study [11]; the latter is far simpler because rotations and orientations can be separated, which permits one to solve it exactly [12,13]. In spite of being separable, this model reveals important information on the structure of the direct correlation function; for instance, it explicitly shows that conformal approximations will necessarily fail [13].

The separable model can be used as an approximation to the nonseparable one. Their respective equations of state are essentially indistinguishable [14] and the adsorption profiles near a wall are very similar at high pressure or low anisotropy [14]. However, out of this regime, the separable model overestimates the orientation in the bulk and this leads to significant deviations of the adsorption profiles. In this regime nonseparability has observable effects. Truly nonseparable models are difficult to solve analytically [11]. Thus the

aim of this work is to introduce a highly idealized model in which nonseparability is implemented in the simplest possible way and yet the model remains analytically tractable. With the help of this model we will show that despite its implicity it accounts for the differences in the angular profiles far and close to a hard wall and that this corrects for the discrepancies in the adsorption profiles.

The paper is organized as follows. In Sec. II the nonseparable interaction model for the one-dimensional fluid is presented. In Sec. III the analytical expressions for the particle radial and angular density profiles are derived and their asymptotic behavior is discussed. In Sec. IV the Monte Carlo simulation method for the title system is described. In Sec. V the analytical radial and angular density profiles from the present model are worked out for two different interaction potentials and the results are compared to the Monte Carlo profiles and to the prediction of a separable interaction model reported previously. The results are summarized in Sec. VI and final conclusions are drawn.

II. MODEL

Let us consider a system of N freely rotating hard ellipses with their centers of mass restricted to move along a segment of length L. The ellipses interact by means of a nearest-neighbor hard core pair potential of the form

$$\Phi(|x-x'|;\phi,\phi')=\begin{cases}0 & \text{if } |x-x'|>\sigma(\phi,\phi') \\ \infty & \text{if } |x-x'|<\sigma(\phi,\phi'),\end{cases} \tag{1}$$

where $\sigma(\phi,\phi')$ represents the contact distance between two neighboring hard ellipses with orientations ϕ and ϕ', respectively.

Only a limited number of exact results can be obtained for this general problem [11]. On the other hand, it has been shown that the partition function and the properties of this system can be derived analytically if the contact distance is assumed to be separable: $\sigma(\phi,\phi')=\sigma(\phi)+\sigma(\phi')$. Reasonable results are obtained within this approximation for the equation of state as well as the radial and angular density distributions [13,14].

One of the main drawbacks of assuming a separable contact distance is that it leads to a full decoupling between the angular and radial profiles of the particles. Thus the same angular distribution is obtained at all distances from the hard wall. This prediction is in contradiction with the results of the Monte Carlo simulation (and common sense) for the system, where a higher degree of alignment (i.e., a narrower angular density profile around $\phi=0°$) is obtained in the proximity of the hard wall than at large distances from it (bulk limit) as a consequence of the larger concentration of particles [14].

In an attempt to correct for these limitations, in the present work we propose a simple nonseparable model for the hard core interaction whose properties can still be determined analytically. It will be shown that such a model introduces a realistic coupling between the equilibrium angular and radial density profiles.

We assume a nonseparable contact distance of the form

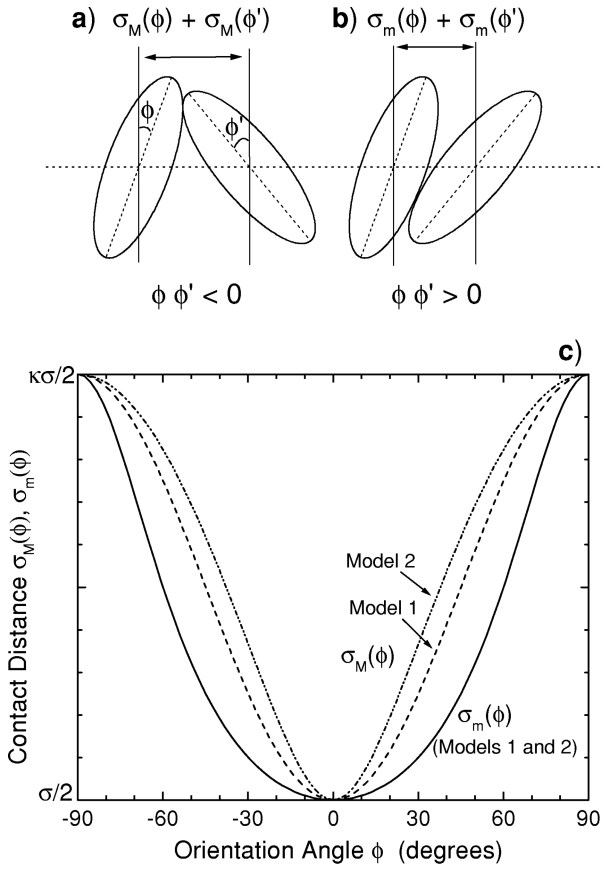

FIG. 1. (a) and (b) Diagrams illustrating the separation between the centers of two neighboring particles at contact for the (a) ''head-to-head'' configuration $[\phi\phi'<0, \sigma(\phi,\phi')=\sigma_M(\phi)+\sigma_M(\phi')]$ and (b) ''parallel'' configuration $[\phi\phi'>0, \sigma(\phi,\phi')=\sigma_m(\phi)+\sigma_m(\phi')]$. (c) Dependence on the orientation angle ϕ of the contact distance functions $\sigma_M(\phi)$ and $\sigma_m(\phi)$ used to construct the two model potentials (models 1 and 2) for the computation of the analytical density profiles [see expressions (37)–(40)].

$$\sigma(\phi,\phi')=\begin{cases}\sigma_m(\phi)+\sigma_m(\phi') & \text{if } \phi\phi'>0 \\ \sigma_M(\phi)+\sigma_M(\phi') & \text{if } \phi\phi'<0,\end{cases} \tag{2}$$

where $\sigma_m(\phi)$ and $\sigma_M(\phi)$ are two different functions that define the effective contact radius of each ellipse. In this way, the contact distance between two neighboring ellipses also depends on their relative orientation. This is probably the simplest nonseparable functional form for $\sigma(\phi,\phi')$ that can be considered, its physical interpretation being that a different type of contact function applies whether both ellipses are in a ''head-to-head'' configuration $[\phi\phi'<0$, Fig. 1(a)] or in a ''parallel'' configuration $[\phi\phi'>0$, Fig. 1(b)]. This is in contrast to any separable interaction model, where ϕ and ϕ' are fully decoupled and then $\sigma(\phi,\phi')=\sigma(-\phi,\phi')=\sigma(\phi,-\phi')$.

The canonical partition function for this system is, as in the separable model [14], that of a system of hard rods with variable (ϕ-dependent) lengths, averaged over all possible orientations, i.e.,

$$Z_N(\beta,L)=\int_{-\pi}^{\pi}\frac{d\phi_1}{2\pi}\cdots\int_{-\pi}^{\pi}\frac{d\phi_N}{2\pi}\int_0^L dx_1\cdots\int_0^L dx_N \times\exp\left\{-\beta\sum_{j=0}^{N}\Phi(|x_j-x_{j+1}|;\phi,\phi')\right\} =\int_{-\pi}^{\pi}\frac{d\phi_1}{2\pi}\cdots\int_{-\pi}^{\pi}\frac{d\phi_N}{2\pi}\frac{1}{N!} \times\left(L-\sum_{j=0}^{N}\sigma(\phi_j,\phi_{j+1})\right)^N \times\Theta\left(L-\sum_{j=0}^{N}\sigma(\phi_j,\phi_{j+1})\right). \quad (3)$$

Here x_j and ϕ_j denote, respectively, the position and the orientation of the jth particle, $\beta=(k_BT)^{-1}$ is the inverse of the absolute temperature in units of the Boltzmann constant, and $\Theta(x)$ is the Heaviside step function, equal to 1 if $x>0$ and 0 if $x<0$.

The boundary conditions imposed by the hard walls at both ends of the segment is implemented in Eq. (3) as the interaction of the first ($j=1$) and last ($j=N$) ellipses with their mirror images. Thus $x_0=-x_1,\phi_0=-\phi_1$, $x_{N+1}=2L-x_N,\phi_{N+1}=-\phi_N$, and, consequently, $\sigma(\phi_0,\phi_1)\equiv\sigma_M(\phi_1)$ and $\sigma(\phi_N,\phi_{N+1})\equiv\sigma_M(\phi_N)$ are defined to represent the contact distances from the first and last particles, respectively, to the walls.

III. DENSITY PROFILES

A. Isobaric ensemble

The one-particle distribution function in the canonical ensemble for the system of hard ellipses near a hard wall is given by

$$\rho_L(x,\phi)\equiv\sum_{k=1}^{N}\langle\delta(x-x_k)\,\delta(\phi-\phi_k)\rangle_{\text{canonical}} =\frac{1}{Z_N(\beta,L)}\sum_{k=1}^{N}\int_{-\pi}^{\pi}\frac{d\phi_1}{2\pi}\cdots\int_{-\pi}^{\pi}\frac{d\phi_N}{2\pi}\frac{(x-\mathcal{F}_k)^{k-1}}{(k-1)!} \times\Theta(x-\mathcal{F}_k)\frac{(L-x-\mathcal{G}_k)^{N-k}}{(N-k)!}\Theta(L-x-\mathcal{G}_k), \quad (4)$$

with

$$\mathcal{F}_k=\mathcal{F}_k(\phi_1,\ldots,\phi_{k-1},\phi) \equiv\sum_{j=0}^{k-2}\sigma(\phi_j,\phi_{j+1})+\sigma(\phi_{k-1},\phi),\quad k=2,\ldots,N \quad (5)$$

$$\mathcal{G}_k=\mathcal{G}_k(\phi,\phi_{k+1},\ldots,\phi_N) \equiv\sigma(\phi,\phi_{k+1})+\sum_{j=k+1}^{N}\sigma(\phi_j,\phi_{j+1}),\quad k=1,\ldots,N-1 \quad (6)$$

$$\mathcal{F}_1=\mathcal{G}_N=\sigma_M(\phi). \quad (7)$$

Note that, in particular, $\mathcal{F}_2=\sigma_M(\phi_1)+\sigma(\phi_1,\phi)$ and $\mathcal{G}_{N-1}=\sigma(\phi,\phi_N)+\sigma_M(\phi_N)$ because of the interactions with the walls.

The analytical computation of the density function is more conveniently performed in the isobaric ensemble as

$$\rho_P(x,\phi)\equiv\sum_{k=1}^{N}\langle\delta(x-x_k)\,\delta(\phi-\phi_k)\rangle_{\text{isobaric}} =\frac{1}{Q_N(\beta,P)}\int_0^\infty dL e^{-\beta PL}Z_N(\beta,L)\rho_L(x,\phi) =\frac{1}{Q_N(\beta,P)}\sum_{k=1}^{N}\int_{-\pi}^{\pi}\frac{d\phi_1}{2\pi}\cdots\int_{-\pi}^{\pi}\frac{d\phi_N}{2\pi} \times\frac{(x-\mathcal{F}_k)^{k-1}}{(k-1)!}\Theta(x-\mathcal{F}_k)\frac{e^{-\beta P(x+\mathcal{G}_k)}}{(\beta P)^{N-k+1}}, \quad (8)$$

where $Q_N(\beta,P)$ is the isobaric partition function. Evaluation of $\rho_P(x,\phi)$ as given in Eq. (8) is more easily achieved by Laplace transforming in the position coordinate. For convenience, it is better to transform with respect to the variable $y=x-\sigma_M(\phi)$ (i.e., the position relative to the minimum possible distance of the first particle to the wall for a given ϕ). Thus

$$\tilde{\rho}_P(s,\phi)\equiv\int_0^\infty dy e^{-sy}\rho_P(y,\phi) =\frac{1}{Q_N(\beta,P)}\sum_{k=1}^{N}\int_{-\pi}^{\pi}\frac{d\phi_1}{2\pi}\cdots\int_{-\pi}^{\pi}\frac{d\phi_N}{2\pi} \times\frac{e^{-(\beta P+s)[\mathcal{F}_k-\sigma_M(\phi)]}}{(\beta P+s)^k}\frac{e^{-\beta P[\sigma_M(\phi)+\mathcal{G}_k]}}{(\beta P)^{N-k+1}}. \quad (9)$$

The Laplace transform can be expressed in a more compact form by introducing a transfer-operator formalism

$$\tilde{\rho}_P(s,\phi)=\frac{1}{Q_N(\beta,P)}\sum_{k=1}^{N}\frac{e^{s\sigma_M(\phi)}}{(\beta P)^{N-k+1}(\beta P+s)^k} \times v_s^{\top}\cdot\hat{T}_s^{k-1}\cdot\hat{\Delta}(\phi)\cdot\hat{T}^{N-k}\cdot v, \quad (10)$$

Here $\hat{T}$, $\hat{T}_s$, and $\hat{\Delta}(\phi)$ are integral operators such that, if $\hat{A}$ denotes any one of them, $(\hat{A}\cdot v)(\theta)=\int_0^{\pi/2}(d\theta'/\pi)A(\theta,\theta')v(\theta')$, where $A(\theta,\theta')$ is 2×2 matrix whose elements depend on θ and θ' and v is a two-component column vector with θ'-dependent elements. These are given by the expressions

$$T(\theta,\theta')=\begin{pmatrix} e^{-\beta P[\sigma_m(\theta)+\sigma_m(\theta')]} & e^{-\beta P[\sigma_M(\theta)+\sigma_M(\theta')]} \\ e^{-\beta P[\sigma_M(\theta)+\sigma_M(\theta')]} & e^{-\beta P[\sigma_m(\theta)+\sigma_m(\theta')]}\end{pmatrix}, \quad (11)$$

$$\Delta(\phi;\theta,\theta')=\pi\delta(\phi-\theta)\,\delta(\theta-\theta')\begin{pmatrix}1&0\\0&1\end{pmatrix}, \tag{12}$$

$$v(\theta)=e^{-\beta P\sigma_M(\theta)}\begin{pmatrix}1\\1\end{pmatrix}. \tag{13}$$

The superscript $\top$ denotes vectorial transposition and s is used throughout the text as a subscript or superscript to indicate the dependence on the variable $\beta P+s$ instead of βP [e.g., the exponential factor $e^{-\beta P\sigma_M(\theta)}$ in Eq. (13) for $v(\theta)$ becomes $e^{-(\beta P+s)\sigma_M(\theta)}$ for $v_s(\theta)$].

B. Calculation of $Q_N(\beta,P)$

The isobaric partition function takes the following form within the transfer matrix formalism:

$$\begin{aligned}Q_N(\beta,P)&=\int_0^\infty dL e^{-\beta PL}Z_N(\beta,L)\\&=\frac{1}{(\beta P)^{N+1}}v^\top\cdot\hat{T}^{N-1}\cdot v.\end{aligned} \tag{14}$$

Diagonalization of the operator $\hat{T}$ is carried out in detail in the Appendix. Its spectral decomposition is given by

$$\hat{T}=\sum_{i=1}^{4}\lambda_i f_i\cdot f_i^\top, \tag{15}$$

where λ_i are the four nonzero eigenvalues of $\hat{T}$ and f_i their corresponding eigenvectors. Consequently, the isobaric partition function can be expressed as

$$\begin{aligned}Q_N(\beta,P)&=\frac{1}{(\beta P)^{N+1}}\sum_{i=1}^{4}\lambda_i^{N-1}(v\cdot f_i)^2\\&=\frac{1}{(\beta P)^{N+1}}\lambda_1^N\left|\frac{\lambda_1-I_m}{\lambda_1-\dfrac{I_M+I_m}{2}}\right|\left\{1+O\left(\left(\frac{\lambda_2}{\lambda_1}\right)^N\right)\right\},\end{aligned} \tag{16}$$

where λ_1 is the eigenvalue with the largest absolute value. See the Appendix for the notation.

C. Calculation of $\tilde{\rho}_P(s,\phi)$

From Eq. (15) the Laplace transform of the density function $\tilde{\rho}_P(s,\phi)$ can be written as

$$\begin{aligned}\tilde{\rho}_P(s,\phi)=\frac{e^{s\sigma_M(\phi)}}{Q_N(\beta,P)}\Bigg\{&\sum_{j=1}^{2}[v_s\cdot\hat{\Delta}(\phi)\cdot f_j](f_j\cdot v)\\&\times\frac{\lambda_j^{N-1}}{(\beta P+s)(\beta P)^N}+\sum_{k=2}^{N-1}\sum_{i,j=1}^{2}(v_s\cdot f_i^s)\\&\times[f_i^s\cdot\hat{\Delta}(\phi)\cdot f_j](f_j\cdot v)\frac{(\lambda_i^s)^{k-1}\lambda_j^{N-k}}{(\beta P+s)^k(\beta P)^{N-k+1}}\\&+\sum_{i=1}^{2}(v_s\cdot f_i^s)[f_i^s\cdot\hat{\Delta}(\phi)\cdot v]\frac{(\lambda_i^s)^{N-1}}{(\beta P+s)^N(\beta P)}\Bigg\},\end{aligned} \tag{17}$$

which, using Eq. (16) for $Q_N(\beta,P)$ and taking the thermodynamic limit $N\to\infty$, becomes

$$\begin{aligned}\tilde{\rho}_P(s,\phi)=\frac{e^{s\sigma_M(\phi)}}{1+\dfrac{s}{\beta P}}\Bigg\{&\frac{v_s\cdot\hat{\Delta}(\phi)\cdot f_1}{v\cdot f_1}+\sum_{i=1}^{2}\frac{\lambda_i^s/\lambda_1}{1+\dfrac{s}{\beta P}-\dfrac{\lambda_i^s}{\lambda_1}}\\&\times\frac{(v_s\cdot f_i^s)[f_i^s\cdot\hat{\Delta}(\phi)\cdot f_1]}{v\cdot f_1}\Bigg\}.\end{aligned} \tag{18}$$

In the derivation we have used that

$$\lim_{N\to\infty}\left(\frac{\lambda_j}{\lambda_1}\right)^{N-1}=\delta_{j,1},\quad \lim_{N\to\infty}\left(\frac{\lambda_j^s\beta P}{\lambda_1(\beta P+s)}\right)^{N-1}=0\quad(s>0). \tag{19}$$

The dot products in Eq. (18) can be readily developed to give

$$\begin{aligned}f_i^s\cdot\hat{\Delta}(\phi)\cdot f_1=\frac{1}{N_i^sN_1}[&I_\times^s e^{-(\beta P+s)\sigma_m(\phi)}\\&+(\lambda_i^s-I_m^s)e^{-(\beta P+s)\sigma_M(\phi)}][I_\times e^{-\beta P\sigma_m(\phi)}\\&+(\lambda_1-I_m)e^{-\beta P\sigma_M(\phi)}],\end{aligned} \tag{20}$$

$$\begin{aligned}v_s\cdot\hat{\Delta}(\phi)\cdot f_1=\frac{\sqrt{2}}{N_1}e^{-(\beta P+s)\sigma_M(\phi)}[&I_\times e^{-\beta P\sigma_m(\phi)}\\&+(\lambda_1-I_m)e^{-\beta P\sigma_M(\phi)}]\end{aligned} \tag{21}$$

(see the Appendix for the notation). Substituting into Eq. (18) and simplifying as appropriate, this results in the expression

$$\begin{aligned}\tilde{\rho}_P(s,\phi)=&\frac{I_\times e^{-\beta P[\sigma_M(\phi)+\sigma_m(\phi)]}+(\lambda_1-I_m)e^{-2\beta P\sigma_M(\phi)}}{\lambda_1^2(\lambda_1-I_m)\left(1+\dfrac{s}{\beta P}-\dfrac{\lambda_1^s}{\lambda_1}\right)\left(1+\dfrac{s}{\beta P}-\dfrac{\lambda_2^s}{\lambda_1}\right)}\\&\times\left[\lambda_1\left(1+\frac{s}{\beta P}\right)-I_m^s+I_\times^s e^{(\beta P+s)[\sigma_M(\phi)-\sigma_m(\phi)]}\right].\end{aligned} \tag{22}$$

D. Density far from the wall (bulk limit)

The expression (22) provides direct information on the behavior of the density function in the limits $y\to\infty$ (bulk) and $y\to 0$ (closest distance to the wall) through the Tauberian theorems [14,15]. Taking the Laplace transform $\tilde{\rho}_P(s,\phi)$ to the limit $s\to 0$ yields the behavior of $\rho_P(y,\phi)$ at large distances from the hard wall (i.e., $y\to\infty$) as

$$\tilde{\rho}_P(s,\phi)\sim \frac{[I_\times e^{-\beta P\sigma_m(\phi)}+(\lambda_1-I_m)e^{-\beta P\sigma_M(\phi)}]^2}{\lambda_1(\lambda_1-I_m)(\lambda_1-\lambda_2)} \times\frac{\beta P}{1-\beta P\left(\dfrac{d\ln\lambda_1^s}{ds}\right)_{s=0}}\frac{1}{s}+O(1)$$

$$=[f_1(\phi)]^2\frac{\beta P}{1-\beta P\left(\dfrac{d\ln\lambda_1^s}{ds}\right)_{s=0}}\frac{1}{s}+O(1). \tag{23}$$

We recall that $f_1(\phi)$ is the eigenvector of the operator $\hat{T}$ corresponding to its largest eigenvalue λ_1 (note that $[f_1(\phi)]^2=f_1^\top(\phi)f_1(\phi)$ does not involve angular integration).

The (normalized) angular distribution $h_{\rm bulk}(\phi)$ and the average density $\langle\rho_{\rm bulk}\rangle$ in the bulk limit are given by

$$\rho_{P,\rm bulk}(\phi)=h_{\rm bulk}(\phi)\langle\rho_{\rm bulk}\rangle, \tag{24}$$

$$h_{\rm bulk}(\phi)=[f_1(\phi)]^2, \tag{25}$$

$$\langle\rho_{\rm bulk}\rangle=\frac{\beta P}{1-\beta P\left(\dfrac{d\ln\lambda_1^s}{ds}\right)_{s=0}}. \tag{26}$$

Equation (26) yields the equation of state of this fluid model.

E. Density at the wall

The determination of the value of $\rho_P(y,\phi)$ at the wall ($y=0$) requires the analysis of the asymptotic behavior of the Laplace transform $\tilde{\rho}_P(s,\phi)$, when $s\to\infty$. A first step is the characterization of the asymptotic form of the functions I_j^s, which are defined as (see the Appendix)

$$I_j^s=\frac{1}{\pi}\int_0^{\pi/2}d\phi e^{-2(\beta P+s)\sigma_j(\phi)},\quad j=m,M,\times, \tag{27}$$

where we have introduced the notation $\sigma_\times(\phi)=[\sigma_m(\phi)+\sigma_M(\phi)]/2$. Since $\sigma_j(\phi)$ are all even functions of ϕ with a single minimum located at $\phi=0$ [where $\sigma_j(0)=\sigma/2$, the minor radius of the molecules], it follows that (when $s\to\infty$)

$$I_j^s\sim\frac{1}{\sqrt{4\pi(\beta P+s)\sigma_j''(0)}}e^{-(\beta P+s)\sigma}. \tag{28}$$

With these expressions for I_j^s one asymptotically obtains

$$\tilde{\rho}_P(s,\phi)\sim\frac{I_\times e^{-\beta P[\sigma_M(\phi)+\sigma_m(\phi)]}+(\lambda_1-I_m)e^{-2\beta P\sigma_M(\phi)}}{\lambda_1(\lambda_1-I_m)}\frac{\beta P}{s} +O\left(\frac{e^{s[\sigma_M(\phi)-\sigma_m(\phi)-\sigma]}}{s^{5/2}}\right). \tag{29}$$

The expression (29) will behave in the limit as C/s provided $\sigma_M(\phi)-\sigma_m(\phi)-\sigma\leqslant 0$; otherwise it will diverge exponentially with s. Note that a Laplace transform of the form $\tilde{g}(s)e^{sa}$ corresponds to a function $g(x)\Theta(x+a)$. Thus an inmediate consequence of the exponentially divergent term is that it would allow for the density to become larger than zero at negative values of $y[=x-\sigma_M(\phi)]$ [up to $\sigma+\sigma_m(\phi)-\sigma_M(\phi)$]. The reason for this anomaly can be found in the fact that the interaction potential we have introduced has a discontinuity of the form

$$\lim_{\phi_1\to 0^-}\sigma(\phi_1,\phi_2)\neq\lim_{\phi_1\to 0^+}\sigma(\phi_1,\phi_2), \tag{30}$$

and likewise for ϕ_2. The physical meaning of this effect is that particles are found at distances from the wall shorter than the minimum allowed $\sigma_M(\phi)$.

Thus the proposed model presents a weak point, which is the price to be paid in order to have a nonseparable model simple enough as to be analytically tractable. Nevertheless, the dominance of the exponential term in Eq. (29) will only occur for values of κ (aspect ratio of the particles, i.e., ratio between the major and minor diameters) above a certain threshold value. In Sec. V it is shown that with an appropiate selection of the contact functions $\sigma_m(\phi)$ and $\sigma_M(\phi)$ the range of validity of the model can be extended over a large interval of aspect ratios.

In turn, for values of the parameters yielding an acceptable physical behavior, i.e., $\tilde{\rho}_P(s,\phi)\propto 1/s$ in the limit $s\to\infty$, the angular profile and the average density at the wall are

$$\rho_{P,\rm wall}(\phi)=h_{\rm wall}(\phi)\langle\rho_{\rm wall}\rangle, \tag{31}$$

$$h_{\rm wall}(\phi)=\frac{I_\times e^{-\beta P[\sigma_M(\phi)+\sigma_m(\phi)]}+(\lambda_1-I_m)e^{-2\beta P\sigma_M(\phi)}}{\lambda_1(\lambda_1-I_m)}, \tag{32}$$

$$\langle\rho_{\rm wall}\rangle=\beta P. \tag{33}$$

Equation (33) is the well-known sum rule that is fulfilled by any fluid at contact with a hard wall.

F. Inversion of $\tilde{\rho}_P(s,\phi)$

Calculation of $\rho_P(y,\phi)$ from the Laplace inversion of $\tilde{\rho}_P(s,\phi)$ is a difficult task that must be performed numerically. We construct for this purpose the Fourier transform of the density function $\hat{\rho}_P(q,\phi)$, which is obtained from the Laplace transform in a straightforward way through the simple relationship

$$\hat{\rho}_P(q,\phi)=\tilde{\rho}_P(iq,\phi)+\tilde{\rho}_P(-iq,\phi). \tag{34}$$

Equation (34) holds for Laplace transforms with no singularities, something that $\tilde{\rho}_P(s,\phi)$ violates [it is singular for $s=0$; see Eq. (22)]. This divergence expresses that $\rho_P(y,\phi)$ tends to a nonzero value for $y\to\infty$ [Eq. (24)] and therefore it is not integrable. However, this difficulty can be easily circumvented by applying Eq. (34) to the adsorption function $\rho_P^{\text{ads}}(y,\phi)=\rho_P(y,\phi)-\rho_P(\infty,\phi)=\rho_P(y,\phi)-\rho_{\text{bulk}}(\phi)$. It follows that

$$\rho_P^{\text{ads}}(y,\phi)=\frac{1}{\pi}\int_0^\infty dq\,\cos(qy)\hat{\rho}_P(q,\phi)$$

$$=\frac{2}{\pi}\int_0^\infty dq\,\cos(qy)\text{Re}[\tilde{\rho}_P(iq,\phi)], \qquad (35)$$

where $\text{Re}[\xi]$ denotes the real part of the complex argument ξ.

The density profiles $\rho_P(y,\phi)$ are finally obtained by numerically transforming back the expression (35) with an appropiate choice of contact distance functions $\sigma_M(\phi)$ and $\sigma_m(\phi)$. The results of the computations are presented in Sec. V, where they are compared with the Monte Carlo simulations of the system.

IV. MONTE CARLO SIMULATIONS

In order to test the performance of the analytical model we have carried out Monte Carlo simulations for the hard ellipse system confined in a segment bounded by hard walls. The simulations, performed in the isothermal-isobaric ensemble (T,P,N constant) [16], follow the methodology developed for hard rods in Ref. [17]. Forbidden system configurations are those in which any two ellipses overlap. In this way, a Monte Carlo trial consists of moving simultaneously both the position x_i and the orientation ϕ_i of the ith particle. This is done by adding two random quantities Δx and $\Delta\phi$, uniformly chosen within the intervals $(-\Delta,\Delta)$ and $(-\Delta',\Delta')$, respectively. The resulting configuration is rejected if it implies an overlap of the ith particle with any of its nearest neighbors, which is tested according to Vieillard-Baron's criterion [18]. The displacement variation intervals (Δ,Δ') have been chosen in such a way that the acceptance ratio is around 20–30 %.

After going through trial angular/position displacements over all particles once, an attempt to change the length of the segment L is performed. In this case, the new length is obtained after multiplying the current length by a factor $\exp(\chi_L)$, where χ_L is a random number uniformly distributed in the interval $(-\chi,\chi)$. This change is rejected if an overlap occurs and accepted otherwise with a probability

$$r\equiv\min\{1,\exp[(N+1)\chi_L-\beta PL(\exp(\chi_L)-1)]\}. \qquad (36)$$

The value of χ is again chosen such that the length-change acceptance ratio is about 20–30 %. The reason for sampling $\ln L$ instead of L is that the domain of the generated random chain coincides with the range of acceptable values of L ($L>0$), thus improving the efficiency of the sampling [16,19]. Furthermore, the changes of L have been performed keeping one wall fixed and moving the other wall [17]. This procedure reduces the number of particles needed, as it directly provides an asymmetric density profile.

Since the analytical model has been worked out in terms of the displaced position variable y (see Sec. III A), a similar coordinate shift was applied in the Monte Carlo simulation: $y_i=x_i-\sigma(\phi_i)$, where $\sigma(\phi_i)$ is the exact contact distance of the first particle to the wall, for an orientation ϕ_i [this is given by the expression (39) below]. The shifted position y_i was stored for the statistical averaging.

The Monte Carlo computation was run with ten particles after we verified that such a number was sufficient to reproduce the density profiles in the whole range of interest. The system was allowed to thermalize with 10^4 Monte Carlo steps (one step meaning N Monte Carlo trials plus an attempt of changing the system length) and the actual averaging was computed over 10^7 additional steps.

V. RESULTS

A. Contact distance functions

Density profiles as a function of the orientation angle ϕ and the particle-wall distance y have been computed numerically from Eq. (35) for several pressures and particle aspect ratios. Two different sets of contact distance functions $\sigma_M(\phi),\sigma_m(\phi)$ have been chosen in order to test the present model. The first series of calculations was carried out with the expressions (henceforth model 1)

$$\sigma_M(\phi)=\frac{\sigma}{2}\left[\frac{\kappa+1}{2}-\frac{\kappa-1}{2}\cos(2\phi)\right], \qquad (37)$$

$$\sigma_m(\phi)=\frac{\sigma}{2}\kappa\left[\frac{\kappa+1}{2}+\frac{\kappa-1}{2}\cos(2\phi)\right]^{-1}, \qquad (38)$$

where σ and $\kappa\sigma$ are, respectively, the minor and major diameters of the particle. The expression (37) for $\sigma_M(\phi)$ is the same function suggested in previous separable interaction studies [13,11]. The choice of the expression (38) for $\sigma_m(\phi)$ was made in order to ensure a smaller contact distance for the parallel configuration than for the head-to-head one (see Fig. 1) while fulfilling the constraints $\sigma_m(0°)=\sigma_M(0°)=\sigma/2$ and $\sigma_m(90°)=\sigma_M(90°)=\kappa\sigma/2$. The angular dependence of $\sigma_M(\phi)$ and $\sigma_m(\phi)$ for this model is represented in Fig. 1(c).

In order to test the influence of the interaction potential on the angular orientation and on the radial profiles of the particles, a second series of calculations was carried out with a different pair of contact distance functions (henceforth model 2)

$$\sigma_M(\phi)=\frac{\sigma}{2}[\kappa^2\sin^2(\phi)+\cos^2(\phi)]^{1/2}, \qquad (39)$$

$$\sigma_m(\phi)=\frac{\sigma}{2}\kappa\left[\frac{\kappa+1}{2}+\frac{\kappa-1}{2}\cos(2\phi)\right]^{-1}. \qquad (40)$$

The head-to-head contact distance $\sigma_M(\phi)$ in model 2 is given by the analytical value of the ellipse's projection on the x axes. As it can be seen in Fig. 1(c), this choice of

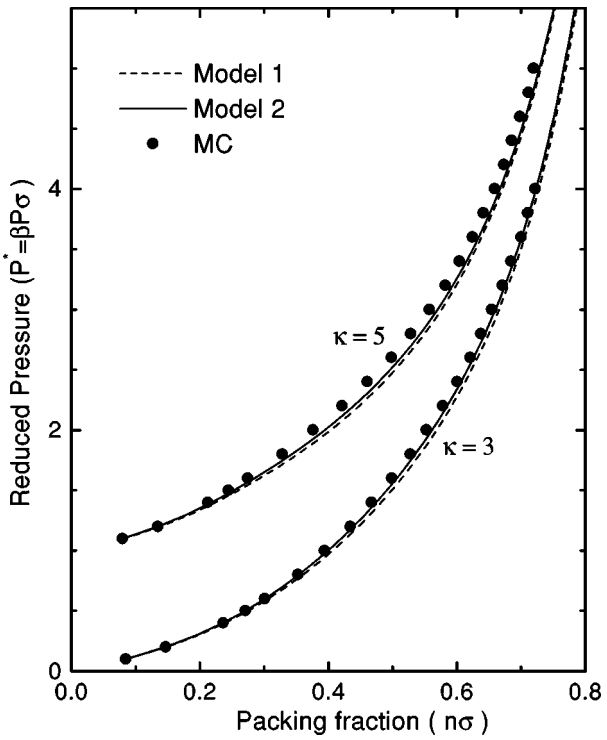

FIG. 2. Reduced pressure $P^* \equiv \beta P \sigma$ versus packing fraction $\eta = \langle \rho_{\text{bulk}} \rangle \sigma$ for aspect ratios $\kappa = 3$ and 5, as obtained from Eq. (41). Circles are the Monte Carlo results, whereas the lines are the analytical profiles (model 1, dashed lines; model 2, solid lines). For the sake of clarity the curves for $\kappa = 5$ are shifted upward by 1.0 units.

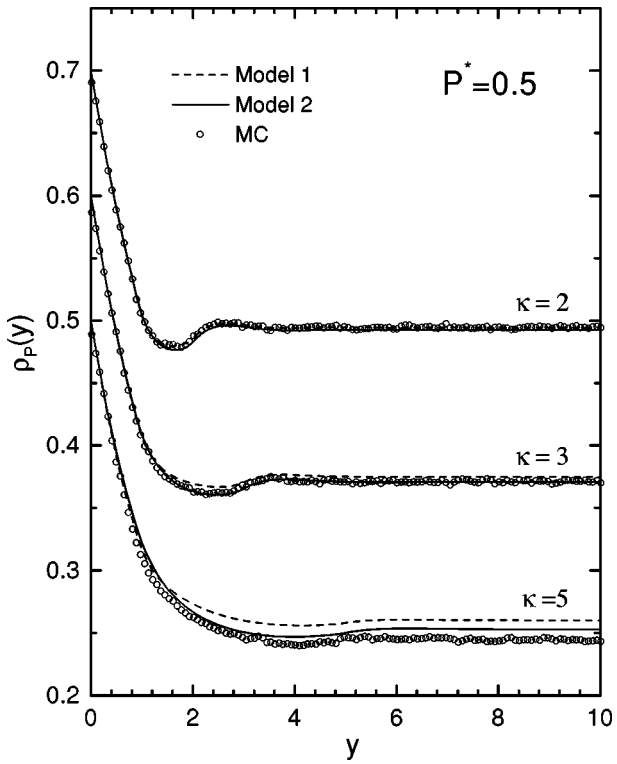

FIG. 3. Radial density profiles at constant pressure $\rho_P(y) \equiv \langle \rho_P(y,\phi) \rangle_\phi$ as a function of y, the position relative to the closest distance of the first particle to the wall (see the text), computed for a reduced pressure $P^* \equiv \beta P \sigma = 0.5$ and aspect ratios $\kappa = 2$, 3, and 5. Circles are the Monte Carlo results, whereas the lines are the analytical profiles (model 1, dashed lines; model 2, solid lines). For the sake of clarity the curves are shifted upward by 0.1 ($\kappa = 3$) and 0.2 ($\kappa = 2$) units.

$\sigma_M(\phi)$ increases the range of the interaction potential with respect to model 1. On the other hand, $\sigma_m(\phi)$ is kept unchanged from model 1.

The condition $\sigma_M(\phi) - \sigma_m(\phi) - \sigma \leqslant 0$, required for the asymptotic convergence of Eq. (29), is fulfilled in models 1 and 2 for aspect ratios smaller than $\kappa_{\max} = 5.8$ and 5.0, respectively. Nevertheless, both models are found to perform reasonably well for κ as large as 10, with the only inconsistency of yielding a value of the particle density at the wall about 10% larger than the correct value $\rho_P(y=0) = \beta P$.

B. Equation of state

The analytical equation of state for the system follows from the expression (26):

$$\frac{1}{\langle \rho_{\text{bulk}} \rangle} = \frac{1}{\beta P} - \left(\frac{d \ln \lambda_1^s}{ds} \right)_{s=0}. \tag{41}$$

Note that the equation of state for the separable interaction model $\langle \rho_{\text{bulk}} \rangle^{-1} = (\beta P)^{-1} - \langle \sigma(\phi) \rangle$ [14,13] is obtained from Eq. (41) in a straightforward way by just taking the particular case $\sigma_M(\phi) = \sigma_m(\phi) \equiv \sigma(\phi)$.

In Fig. 2 we represent the reduced pressure $P^* \equiv \beta P \sigma$ versus the packing fraction $\eta = \langle \rho_{\text{bulk}} \rangle \sigma$ for aspect ratios $\kappa = 3$ and 5, as obtained from Eq. (41), within the present models 1 and 2. The agreement between the analytical and the Monte Carlo results, also shown in the same figure, is very good. This is not too surprising because, in general, the equation of state does not strongly depend on the details of the interaction potential.

C. Radial profiles

Radial density profiles $\rho_P(y)$ have been obtained by averaging $\rho_P(y,\phi)$ over all angles ϕ. Such profiles are more sensitive than the equation of state to fine details of the interaction between the particles and thus provide a more crucial test for the analytical model. Figures 3–6 compare model 1 and model 2 radial profiles with the Monte Carlo ones for several values of the reduced pressure ($P^* \equiv \beta P \sigma = 0.5$, 1, 2, and 4) and the aspect ratio ($\kappa = 2$, 3, and 5).

As it can be seen in these figures, the particles develop a radial layering in the vicinity of the hard wall that becomes progressively more structured as the system pressure increases. The aspect ratio of the particles, on the other hand, does not affect considerably the shape of the radial profiles except for low pressures. The main effect of increasing κ is twofold: a smoothing out of the layered structure of $\rho_P(y,\phi)$ and a shift of the layers toward larger distances from the wall.

The best agreement between the analytical and the Monte Carlo profiles is obtained in the limits of high pressure and small aspect ratio. The same trend was found for the separable interaction model [14]. Indeed, for $\kappa = 2$ model 1 and

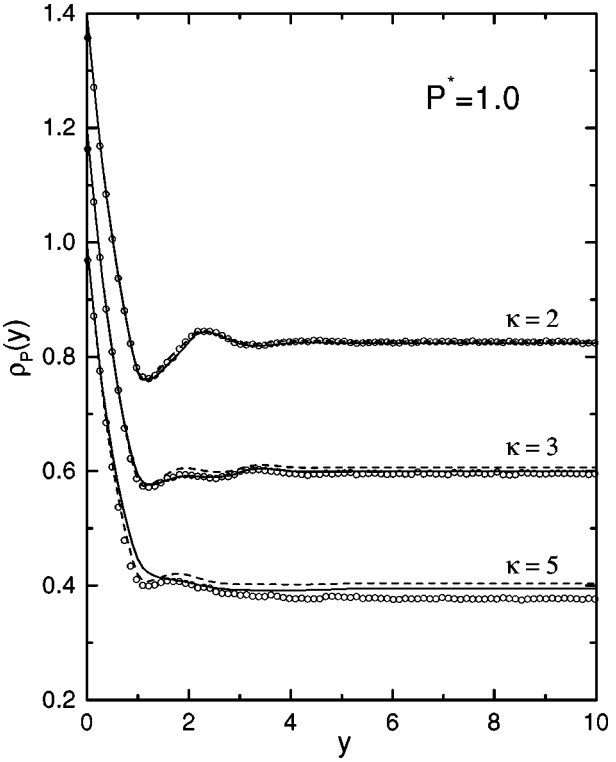

FIG. 4. Same as Fig. 3 for a reduced pressure $P^*\equiv\beta P\sigma=1.0$. For the sake of clarity the curves are shifted upward by 0.2 ($\kappa=3$) and 0.4 ($\kappa=2$) units.

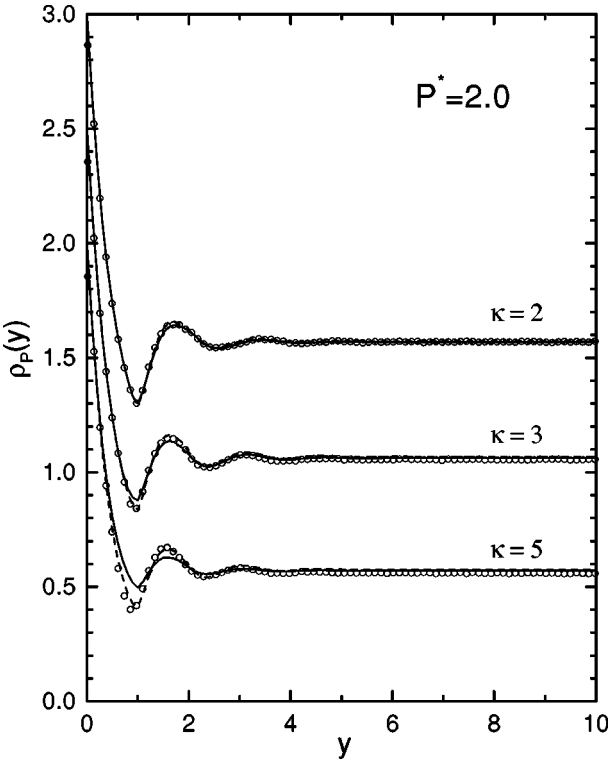

FIG. 5. Same as Fig. 3 for a reduced pressure $P^*\equiv\beta P\sigma=2.0$. For the sake of clarity the curves are shifted upward by 0.5 ($\kappa=3$) and 1.0 ($\kappa=2$) units.

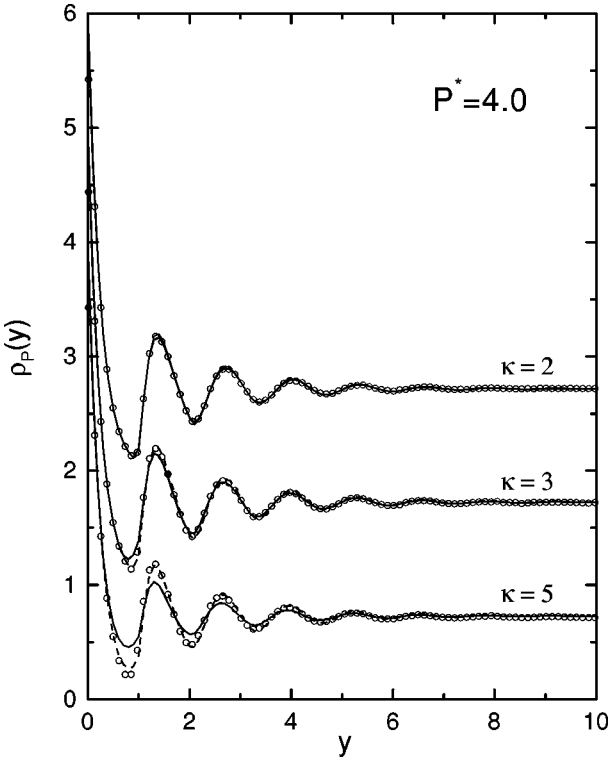

FIG. 6. Same as Fig. 3 for a reduced pressure $P^*\equiv\beta P\sigma=4.0$. For the sake of clarity the curves are shifted upward by 1.0 ($\kappa=3$) and 2.0 ($\kappa=2$) units.

model 2 analytical radial profiles are virtually indistinguishable from the Monte Carlo curves at all four pressures. Furthermore, at high pressure ($P^*\geqslant 2$) model 1 displays an excellent performance even for aspect ratios as large as $\kappa=5$, whereas model 2 yields profiles somewhat smoother (i.e., less structured) than its model 1 and Monte Carlo counterparts, although it still reproduces correctly the position of the layers in the vicinity of the hard wall.

Interestingly, this trend tends to reverse in the low-pressure limit and so at $P^*=0.5$ (Fig. 3) model 2 resembles overall more closely than model 1 the structure of the Monte Carlo radial profiles, especially for high κ. It is noticed as well that, at low pressure, model 2 yields better results than model 1 for the particle density in the bulk limit.

D. Angular profiles

Model 1 and model 2 one-particle ϕ distributions are now compared to the results of the Monte Carlo computation and to the earlier separable model for the system [14]. Figures 7–10 depict a selection of angular profiles in the two limiting cases: in the bulk [Eq. (25)] and at the wall [Eq. (32)].

A remarkable contribution of the present nonseparable interaction model is that it corrects for one of the major inconsistencies of the separable approximation, namely, that the latter factorizes the radial and angular variables of $\rho_P(y,\phi)$, thus yielding the same angular distribution for the particles at all distances from the wall [14]. As shown in Sec. III, such a factorization does not take place in the present model due to the nonseparable nature of the contact distance function. We show below that this feature leads to a more realistic description for the behavior of the hard ellipse system.

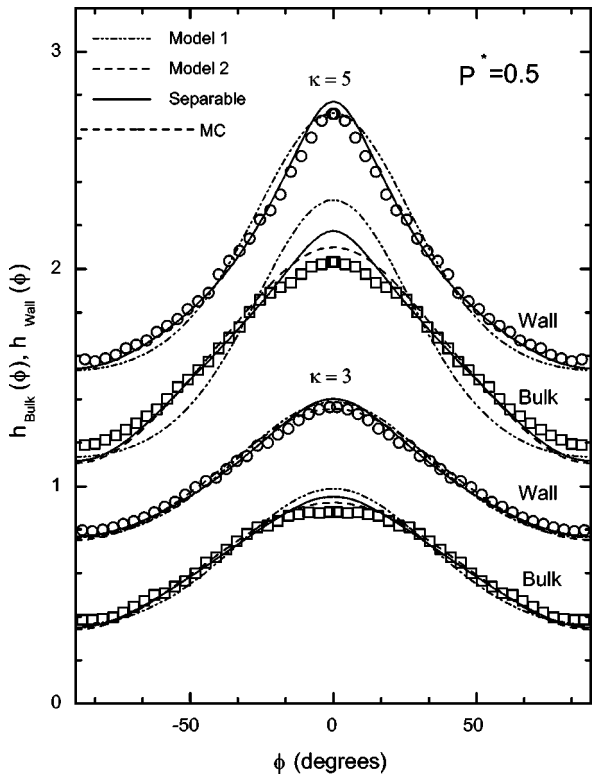

FIG. 7. Normalized angular distributions of the particles at the wall $h_{\mathrm{wall}}(\phi)\equiv\rho_P(y=0,\phi)/\rho_P(y=0)$ and in the bulk $h_{\mathrm{bulk}}(\phi)\equiv\rho_P(y=\infty,\phi)/\rho_P(y=\infty)$, as a function of the molecular orientation ϕ, computed for a reduced pressure $P^*\equiv\beta P\sigma=0.5$ and aspect ratios $\kappa=2$, 3, and 5. Circles and squares are the Monte Carlo distributions at the wall and in the bulk, respectively, whereas the lines are the analytical profiles (model 1, dashed lines; model 2, solid lines; separable model of Ref. [14], dot-dashed lines). For the sake of clarity the curves are shifted upward by 0.4 ($\kappa=3$, wall), 0.95 ($\kappa=5$, bulk), and 1.35 ($\kappa=5$, wall) units.

As it can be seen in the figures, the angular distribution of the particles is broadest (i) at large distance from the hard wall, (ii) for small values of κ, and (iii) at low pressure. Thus the weakest ϕ dependence among the curves in Figs. 7–10 is found in the bulk distribution at $\kappa=3$, $P^*=0.5$, where the probability is Gaussian-like with a full width at half maximum of approximately 60° and its value changes by roughly 50% from $\phi=0°$ to $\phi=90°$. On the other hand, the degree of alignment of the particles increases progressively as κ and P^* increase and y diminishes. At $P^*=4$ (Fig. 10), the angular profiles at the wall for $\kappa=3$ and 5 have much smaller full widths at half maximum, of approximately 30° and 15°, respectively.

For small aspect ratios ($\kappa=2$ and 3) both models 1 and 2 yield broad ϕ distributions that do not change appreciably from the wall to the bulk and are in very good agreement with the Monte Carlo calculation in all cases. For larger κ values, a stronger dependence on the distance to the wall is observed, the angular profile being significantly narrower at the wall than in the bulk. Furthermore, for large aspect ratios the performance of the two sets of contact distance functions (models 1 and 2) becomes clearly differentiated, especially at the wall, where the free mobility of the particles is smallest. The model 2 angular distribution at the wall for $\kappa=5$ is in remarkable agreement with the Monte Carlo values at all

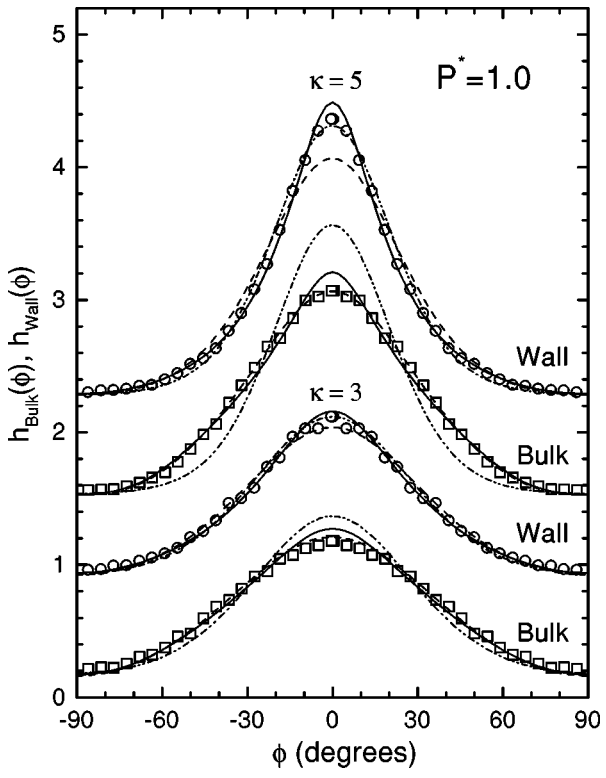

FIG. 8. Same as Fig. 7 for a reduced pressure $P^*\equiv\beta P\sigma=1.0$. For the sake of clarity the curves are shifted upward by 0.75 ($\kappa=3$, wall), 1.5 ($\kappa=5$, bulk), and 2.25 ($\kappa=5$, wall) units.

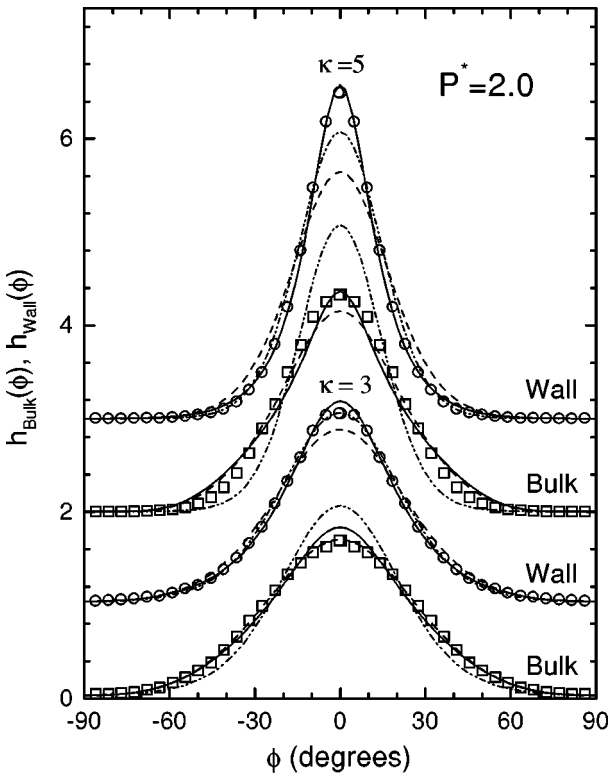

FIG. 9. Same as Fig. 7 for a reduced pressure $P^*\equiv\beta P\sigma=2.0$. For the sake of clarity the curves are shifted upward by 1.0 ($\kappa=3$, wall), 2.0 ($\kappa=5$, bulk), and 3.0 ($\kappa=5$, wall) units.

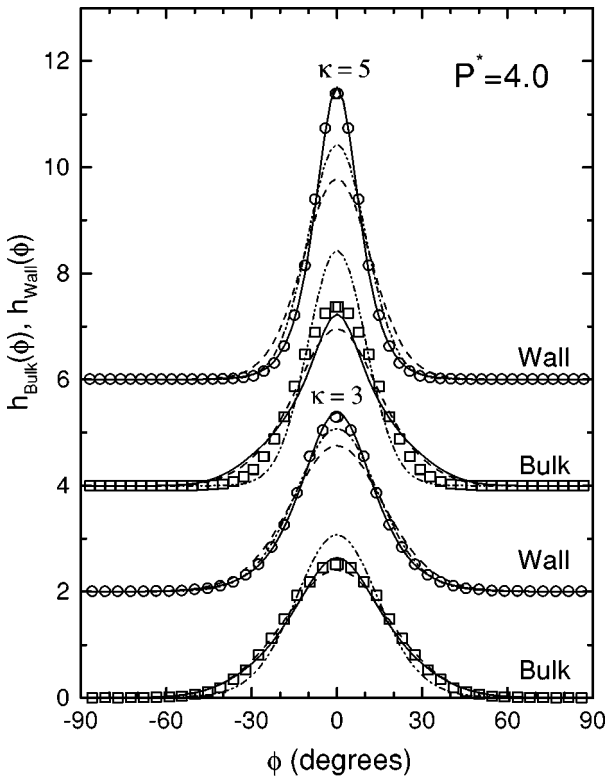

FIG. 10. Same as Fig. 7 for a reduced pressure $P^*\equiv\beta P\sigma=4.0$. For the sake of clarity the curves are shifted upward by 2.0 ($\kappa=3$, wall), 4.0 ($\kappa=5$, bulk), and 6.0 ($\kappa=5$, wall) units.

pressures. Model 1, on the other hand, yields a broader distribution at the wall, which underestimates the degree of alignment of the particles. Finally, models 1 and 2 yield similar results in the bulk limit in all cases. Both models reproduce well the Monte Carlo bulk angular profiles at low pressure, whereas they tend to be somewhat broader at high pressure.

It is interesting to notice that the ϕ distribution obtained within the separable approximation lies in every case very close to that of model 2 and the Monte Carlo curves *at the wall*. On the other hand, the separable model profile does not properly resemble the angular distribution in the bulk, especially for large values of κ. In fact, in Ref. [14] it was shown that if the separable model calculation is performed for a smaller aspect ratio $\kappa_{eff}\approx\kappa^{4/5}$, the resulting (broader) angular distribution is in good agreement with the corresponding Monte Carlo distribution in the bulk. It becomes apparent that one of the main advantages of the present nonseparable treatment is that the coupled angle-radial distributions allow for a study of the correlation between the alignment and the mobility of the particles in a natural way.

VI. CONCLUSIONS

We have presented an analytically solvable nonseparable interaction model for a one-dimensional fluid of anisotropic molecules near a hard wall. In spite of the simplicity, the model provides a very good description for the equation of state of the system and for more sensitive properties, such as the radial and angular profiles of the particles. In particular, the nonseparable character of the particle interaction potential leads to a coupling of the radial and angular parts of the one-body distribution and hence predicts a higher degree of alignment for the particles in the vicinity of the hard wall than at large distances from it, in close agreement with the Monte Carlo results. This feature constitutes a remarkable qualitative improvement with respect to any separable interaction model that necessarily yields the same angular distribution function at all distances from the wall.

Two different sets of hard core potentials have been tested in order to probe the sensitivity of the properties of the system to the shape of the interaction between the particles. The first pair of contact-distance functions (model 1) provides a very accurate description of the particle radial profiles except in the limit of low pressure and high aspect ratio where the fluctuation of the particle orientations become large. A second set of contact-distance functions (model 2) reproduces remarkably well the wall and bulk angular distributions of the particles in all cases, although it leads to a slightly less satisfactory description of the radial profiles. We conclude that, with an appropiate selection of the contact distance functions, the present nonseparable model provides a realistic analytical description of the properties of a typical one-dimensional hard body system.

ACKNOWLEDGMENTS

B. M.-H. acknowledges a grant from the program ''Incorporación a España de Doctores y Tecnólogos'' of the Spanish Ministerio de Educación y Cultura. We acknowledge financial support from the Dirección General de Enseñanza Superior under Projects Nos. PB96-0148 (J. M. P.) and PB96-0119 (J. A. C.).

APPENDIX: DIAGONALIZATION OF THE OPERATOR $\hat{T}$

The eigenvalue equation for the operator $\hat{T}$ defined in Eq. (11) has the form

$$(\hat{T}\cdot f)(\theta)=\int_0^{\pi/2}\frac{d\theta'}{\pi}\begin{pmatrix}A(\theta)A(\theta') & B(\theta)B(\theta')\\ B(\theta)B(\theta') & A(\theta)A(\theta')\end{pmatrix}\begin{pmatrix}u(\theta')\\ w(\theta')\end{pmatrix}=\lambda\begin{pmatrix}u(\theta)\\ w(\theta)\end{pmatrix},\tag{A1}$$

with

$$f(\theta)=\begin{pmatrix}u(\theta)\\ w(\theta)\end{pmatrix},\quad A(\theta)\equiv e^{-\beta P\sigma_m(\theta)},\quad B(\theta)\equiv e^{-\beta P\sigma_M(\theta)}.\tag{A2}$$

Equation (A1) can be rewritten as

$$A(\theta)\int_0^{\pi/2}\frac{d\theta'}{\pi}A(\theta')u(\theta')+B(\theta)\int_0^{\pi/2}\frac{d\theta'}{\pi}B(\theta')w(\theta')=\lambda u(\theta),$$

$$B(\theta)\int_0^{\pi/2}\frac{d\theta'}{\pi}B(\theta')u(\theta') + A(\theta)\int_0^{\pi/2}\frac{d\theta'}{\pi}A(\theta')w(\theta')=\lambda w(\theta). \quad \text{(A3)}$$

Provided $\lambda\neq 0$, it follows that $u(\theta)=\alpha A(\theta)+\beta B(\theta)$ and $w(\theta)=\alpha' A(\theta)+\beta' B(\theta)$ and therefore Eq. (A3) turns into

$$\begin{pmatrix} I_m & I_\times & 0 & 0 \\ 0 & 0 & I_\times & I_M \\ 0 & 0 & I_m & I_\times \\ I_\times & I_M & 0 & 0 \end{pmatrix}\begin{pmatrix}\alpha\\ \beta\\ \alpha'\\ \beta'\end{pmatrix}=\lambda\begin{pmatrix}\alpha\\ \beta\\ \alpha'\\ \beta'\end{pmatrix}, \quad \text{(A4)}$$

where the following notation has been introduced, which is used throughout the present work:

$$I_m=\int_0^{\pi/2}\frac{d\phi}{\pi}e^{-2\beta P\sigma_m(\phi)}, \quad \text{(A5)}$$

$$I_M=\int_0^{\pi/2}\frac{d\phi}{\pi}e^{-2\beta P\sigma_M(\phi)}, \quad \text{(A6)}$$

$$I_\times=\int_0^{\pi/2}\frac{d\phi}{\pi}e^{-\beta P[\sigma_m(\phi)+\sigma_M(\phi)]}. \quad \text{(A7)}$$

Equation (A4) has four (nonzero) eigenvalues

$$\lambda_{1,2}=\frac{I_m+I_M}{2}\pm\left[\left(\frac{I_m-I_M}{2}\right)^2+I_\times^2\right]^{1/2}, \quad \text{(A8)}$$

$$\lambda_{3,4}=\frac{I_m-I_M}{2}\pm\left[\left(\frac{I_m+I_M}{2}\right)^2-I_\times^2\right]^{1/2}. \quad \text{(A9)}$$

The eigenvalues $\lambda_{1,2,3,4}$ have the following algebraic properties (useful for the derivation of the expressions presented in this work): (i) $\lambda_1>\lambda_{2,3,4}$; (ii) $q_i\lambda_i(\lambda_i-I_m)=I_\times^2+I_M(\lambda_i-I_m)$, with $q_1=q_2=+1$ and $q_2=q_3=-1$; (iii) $\lambda_1\lambda_2=-\lambda_3\lambda_4=I_mI_M-I_\times^2\geqslant 0$; (iv) $(\lambda_1-I_m)(\lambda_2-I_m)=-(\lambda_3-I_m)(\lambda_4-I_m)=-I_\times^2$; (v) the eigenvector corresponding to the eigenvalue λ_i is

$$f_i(\phi)=\frac{1}{N_i}\{I_\times e^{-\beta P\sigma_m(\phi)}+(\lambda_i-I_m)e^{-\beta P\sigma_M(\phi)}\}\begin{pmatrix}\frac{1}{\sqrt{2}}\\ \\ \frac{q_i}{\sqrt{2}}\end{pmatrix},$$

where $N_i=|\lambda_i(\lambda_i-I_m)(2\lambda_i-q_iI_M-I_m)|^{1/2}$ is a normalization constant; (vi) the eigenvectors are orthonormal: $f_i\cdot f_j=\int_0^{\pi/2}(d\phi/\pi)f_i^\top(\phi)f_j(\phi)=\delta_{i,j}$; and (vii) the dot products $v\cdot f_i=\int_0^{\pi/2}(d\phi/\pi)v^\top(\phi)f_i(\phi)$ can be expressed as

$$v\cdot f_{1,2}=\frac{\sqrt{2}}{N_{1,2}}\lambda_{1,2}(\lambda_{1,2}-I_m) =\epsilon_{1,2}\left|\frac{\lambda_{1,2}(\lambda_{1,2}-I_m)}{\lambda_{1,2}-\frac{I_M+I_m}{2}}\right|^{1/2}\quad(\epsilon_1=+1,\ \epsilon_2=-1), \quad \text{(A10)}$$

$$v\cdot f_{3,4}=0. \quad \text{(A11)}$$

Equation (A3) has also the solution $\lambda_0=0$. In this case, any two functions $u(\theta),w(\theta)$, belonging to the space orthogonal to the one spanned by the functions $A(\theta)$ and $B(\theta)$ will be a solution of Eq. (A3) with $\lambda_0=0$. Note that, although the subspace spanned by $\lambda_0=0$ is of infinite dimension, its contribution to the spectral decomposition is identically zero.

[1] J. K. Percus, J. Stat. Phys. **89**, 249 (1997).
[2] R. J. Baxter, *Exactly Solved Models in Statistical Mechanics* (Academic, New York, 1982).
[3] Lord Rayleigh, Nature (London) **45**, 80 (1891).
[4] L. Tonks, Phys. Rev. **50**, 955 (1936).
[5] Z. W. Salsburg, J. G. Kirkwood, and R. W. Zwanzig, J. Chem. Phys. **21**, 1098 (1953).
[6] J. K. Percus, J. Stat. Phys. **15**, 505 (1976).
[7] J. K. Percus, J. Stat. Phys. **28**, 67 (1982).
[8] For a relatively recent review see R. Evans, in *Fundamentals of Inhomogeneous Fluids*, edited by D. Henderson (Dekker, New York, 1992).
[9] J. K. Percus and M. Q. Zhang, J. Stat. Phys. **69**, 347 (1990).
[10] E. Kierlik and M. L. Rosinberg, J. Stat. Phys. **68**, 1037 (1992).
[11] J. L. Lebowitz, J. K. Percus, and J. Talbot, J. Stat. Phys. **49**, 1221 (1987).
[12] J. F. Marko, Phys. Rev. Lett. **62**, 543 (1989).
[13] C. F. Tejero and J. A. Cuesta, Physica A **168**, 942 (1990).
[14] F. S. Ferrero, B. Martínez-Haya, J. M. Pastor, J. A. Cuesta, and C. F. Tejero, Mol. Phys. **79**, 709 (1993).
[15] S. Kotz and N. L. Johnson, *Encyclopedia of Statistical Sciences* (Wiley, New York, 1988), Vol. 9.
[16] M. P. Allen and D. J. Tildesley, *Computer Simulation of Liquids* (Oxford University Press, Oxford, 1989).
[17] J. E. Finn and P. A. Monson, Mol. Phys. **65**, 1345 (1988).
[18] J. Vieillard-Baron, J. Chem. Phys. **56**, 4729 (1972).
[19] R. Eppenga and D. Frenkel, Mol. Phys. **52**, 1303 (1984).